RSC Advances

PAPER

View Article Online
View Journal | View Issue

Cite this: *RSC Adv.*, 2022, **12**, 11084

Room-temperature growth of fluorapatite/$CaCO_3$ heterogeneous structured composites inspired by human tooth†

Yidi Li,[a] Hang Ping,[a] Liwen Lei,[a] Jingjing Xie,[a] Zhaoyong Zou,[a] Weimin Wang,[a] Kun Wang *[b] and Zhengyi Fu *[a]

Organisms can synthesize heterogeneous structures with excellent mechanical properties through mineralization, the most typical of which are teeth. The tooth is an extraordinarily resilient bi-layered material that is composed of external enamel perpendicular to the tooth surface and internal dentin parallel to the tooth surface. The synthesis of enamel-like heterostructures with good mechanical properties remains an elusive challenge. In this study, we applied a biomimetic mineralization method to grow fluorapatite/$CaCO_3$ (FAP/$CaCO_3$) heterogeneous structured thin films that mimic their biogenic counterparts found in teeth through a three-step pathway: coating a polymer substrate, growing a layered calcite film, and mineralization of a fluorapatite columnar array on the calcite layer. The synthetic heterostructure composites combine well and exhibit good mechanical properties comparable to their biogenic counterparts. The FAP/$CaCO_3$ heterogeneous structured composite exhibits excellent mechanical properties, with a hardness and Young's modulus of 1.99 ± 0.02 GPa and 47.5 ± 0.6 GPa, respectively. This study provides a reasonable new idea for unique heterogeneous structured materials designed at room temperature.

Received 18th January 2022
Accepted 25th March 2022

DOI: 10.1039/d2ra00374k

rsc.li/rsc-advances

1. Introduction

The unique structural design of biological composites at various scales allows them to achieve remarkable mechanical properties using weak basic constituents, such as in scales and shells.[1,2] With a highly mineralized outer layer that can resist penetration and a tougher lower layer with a twisted arrangement of mineralized collagen fibrils to absorb deformation, scales are some of nature's toughest flexible materials.[3,4] The prismatic-nacreous heterogeneous architecture in mollusc shells has superior non-uniform stress distribution and exhibits toughness and wear-resistance.[5,6] Furthermore, natural structure-forming processes in biological systems, such as biomineralization,[7] can efficiently and accurately fabricate biomaterials under environmentally benign conditions, in contrast to our anthropogenic technologies where harsh conditions are common prerequisites.[8–10] Replication of representative biogenic structural forms using biomimetic mineralization tools is therefore one of the most essential topics in materials science.

The tooth is a remarkably resilient bi-layered material that can withstand mastication forces of over 800 N.[11,12] It derives its structural integrity from its hierarchical architecture that leads to its specific mechanical properties. The tooth consists of two parts: enamel and dentin. Enamel, the outermost layer of the tooth, is one of the most rigid mineralized tissues found in living organisms.[13] It consists of about 96 wt% hydroxyapatite (HA) crystals, 1 wt% organic material and 3 wt% water. Its remarkable mechanical strength and fatigue resistance are attributed to the intricate hierarchical arrangement of nanorod-like HAP crystals oriented perpendicular to the tooth surface.[14,15] The inner layer is dentin, which is composed of a mesh of less mineralized collagen fibers (50% hydroxyapatite) oriented mostly parallel to the tooth surface. The dentin–enamel junction (DEJ), which is the interface between the two layers, displays a gradual transition in the orientation and concentration of such building blocks. Remarkably, this overall architecture typical for teeth shows striking consistency among vertebrates and other species.[15–17] This suggests that the organization of the tooth might have been driven by selective evolutionary pressures that ultimately led to similar and universal design principles.

Due to the excellent mechanical properties of enamel, decades of dedicated research have been directed at replicating its columnar structure and excellent mechanical properties *in*

[a]*State Key Laboratory of Advanced Technology for Materials Synthesis and Processing, Wuhan University of Technology, 122 Luoshi Road, Wuhan, P. R. China. E-mail: zyfu@whut.edu.cn*

[b]*State Key Laboratory of Silicate Materials for Architectures, Wuhan University of Technology, 122 Luoshi Road, Wuhan, P. R. China. E-mail: kun.wang@whut.edu.cn*

† Electronic supplementary information (ESI) available. See https://doi.org/10.1039/d2ra00374k

vitro.[17,18] A hydrothermal technique was used to grow enamel-inspired columnar ZnO or TiO_2 followed by layer-by-layer (LBL) deposition of a polymeric matrix. The hardness and Young's modulus values of the resultant composites were comparable to those of natural enamel. However, most researchers have focused only on the excellent mechanical properties of tooth enamel and have neglected the critical role of dentin whose fracture toughness maintains tooth integrity over time. When a tooth is subjected to external forces, the dentin layer containing partially mineralized collagen fibers oriented parallel to the tooth surface is able to effectively arrest cracks and prevent catastrophic failure of the tooth.

To make an artificial tooth, mineralization is a very promising strategy for optimizing the micro/nanostructures. In the present study, we adopted a bioinspired mineralization technique to fabricate a bi-layered heterostructure to mimic enamel and dentin simultaneously. Calcium carbonate and calcium phosphate are common biological minerals. In this approach, layered calcium carbonate calcite was firstly mineralized *in situ* on chitosan (CS) film. Subsequently, a fluorapatite (FAP) columnar array was grown on the calcite layer under the control of Mg^{2+}. The synthetic FAP/$CaCO_3$ exhibits good mechanical properties with a hardness of 1.99 ± 0.02 GPa and Young's modulus of 47.5 ± 0.6 GPa, which should be attributed to the structural continuity between the FAP layer and $CaCO_3$ layer. This success in turn enriches our mechanistic understanding of biomineralization. Meanwhile, it provides a reliable synthetic approach for biomimetic hybrids with distinct mesostructures and remarkable structural functions under ambient conditions.

2. Experimental

2.1 Materials

$CaCl_2 \cdot 2H_2O$ (M_W = 147), Na_2CO_3 (M_W = 105.9), $Na_2HPO_4 \cdot 12H_2O$ (M_W = 358.14), NaF (M_W = 147), $MgCl_2 \cdot 6H_2O$ (M_W = 203.3) and chitosan (M_W = 310 000) were purchased at analytical grade and used without further purification. PVP (M_n = 60 kg mol^{-1}) and PAA (M_n = 100 kg mol^{-1}) were purchased from Sigma and used as received.

2.2 Polymer coating

Chitosan (CS) (0.5 g) was thoroughly mixed with DIW (49.5 mL), and glacial acetic acid (500 μL) was then added dropwise into the mixture under stirring until a slightly viscous yellowish liquid was formed. The obtained CS solution (1.0 wt%) was degassed by ultrasonic and vacuum treatment. A continuous CS film was deposited on clean glass slides by spin-coating the CS solution (1.0 wt%, 200 μL) at 3000 rpm for 30 s followed by immersing in sodium hydroxide solution (pH = 9) to remove the residual acetic acid.

2.3 Deposition of the calcium carbonate layer

The calcium carbonate layer was deposited *via* mineralization, which involved the slow dripping of solution using a peristaltic pump. A solution of Na_2CO_3 (66.25 mg, 12.5 mM) in deionized water (50 mL) was dripped into a beaker containing a solution of $CaCl_2 \cdot 2H_2O$ (91.87 mg, 12.5 mM), $MgCl_2 \cdot 6H_2O$ (182.97 mg, 18 mM) and 2×10^{-3} wt% PAA in deionized water (50 mL). The dripping was carried out for 18 h using a peristaltic pump with a flow rate of 2.78 mL h^{-1}. The substrates coated with the CS films were positioned at the bottom of the beaker to facilitate the mineralization of the calcium carbonate layer. Subsequently, the calcium carbonate layer, underlying CS thin films, and glass substrate were removed and rinsed with purified water. Thereafter, they were utilized for the characterization of the superimposed mineralization.

2.4 Deposition of the FAP nanorod arrays

A solution of $Na_2HPO_4 \cdot 12H_2O$ (48.3 mg, 2.7 mM) and NaF (5.67 mg, 2.7 mM) in deionized water (50 mL) was dripped into a beaker containing a solution of $CaCl_2 \cdot 2H_2O$ (40 mg, 5.4 mM) and $MgCl_2 \cdot 6H_2O$ (30.5 mg, 3 mM) in deionized water (50 mL). The dripping was carried out for 48 h using a peristaltic pump with a flow rate of 1.04 mL h^{-1}. The substrate with calcium carbonate layers was positioned at the bottom of the beaker to facilitate the mineralization of ACP nanoparticles. Subsequently, the glass substrate was removed and rinsed with purified water.

Then, a solution of $Na_2HPO_4 \cdot 12H_2O$ (48.3 mg, 2.7 mM) and NaF (5.67 mg, 2.7 mM) in deionized water (50 mL) was dripped into a beaker containing a solution of $CaCl_2 \cdot 2H_2O$ (40 mg, 5.4 mM) or $MgCl_2 \cdot 6H_2O$ (11.4 mg, 1.12 mM) in deionized water (50 mL). The dripping was performed for 96 h using a peristaltic pump with a flow rate of 0.52 mL h^{-1}. The substrate with calcium carbonate layers and ACP nanoparticles was positioned at the bottom of the beaker to mineralize the overlayer. Thus, the overgrowth of the FAP nanorod array was realized.

2.5 Characterization

The crystal structures of the samples were investigated *via* XRD (Empyrean, Malvern Panalytical, Malvern, UK) using Cu Kα radiation (λ = 1.54 Å). The 2θ range and scanning speed were 10–80° and 4° min^{-1}, respectively. The bulk thin-film samples were cut into small pieces and then attached to double-sided conductive adhesive tape. A thin layer of gold was deposited on the samples *via* sputter coating for 60 s. The morphological analyses were performed *via* field-emission SEM (FESEM; SU-8020, Hitachi High-Technologies Corporation, Tokyo, Japan) at an acceleration voltage of 5 kV. The TEM samples were prepared *via* FIB milling (Neon 40EsB, ZEISS, Oberkochen, Germany). A bar of SiO_2 was deposited on the samples *via* gas-assisted deposition to protect the surfaces during milling and lift-out. The samples were polished to their final thicknesses (current: 50 pA) after the lift-out and transferred onto the TEM grid. Microstructural analyses were performed *via* TEM and HRTEM (JSM-7100F, Jeol Ltd., Tokyo, Japan). To prepare the samples for analysis, solutions of the FAP/$CaCO_3$ heterogeneous structured composites in ethyl alcohol were dripped onto a carbon-coated 200 mesh copper grid. Imaging was performed after drying the samples under ambient conditions. The chemical bonding states of the FAP/$CaCO_3$ heterogeneous structured composites were investigated *via* XPS analysis (AXIS-

Ultra DLD-600W, Kratos Analytical Limited, Manchester, UK). The samples were also characterized *via* Raman spectroscopy (InVia confocal microscope (equipped with a 633 nm laser), Renishaw plc, Wotton-under-Edge, UK) at 200–1500 cm^{-1}. The functional groups in the columnar-film samples were identified *via* FT-IR spectrometry (Nicolet Nexus (an intelligent spectrometer), Thermo Fisher Scientific, Massachusetts, USA) at 4000–400 cm^{-1}. Thermogravimetric analysis (TGA; STA 449 F3 Jupiter, NETZSCH-Gerätebau GmbH, Selb, Germany) was performed to ascertain the organic–inorganic content of the bulk films. The analysis was performed in air at a heating rate of 5 °C min^{-1} from 25 °C to 1000 °C. The mechanical properties of the FAP/$CaCO_3$ heterogeneous structured composites were determined *via* nanoindentation tests (G200, Keysight Technologies, California, USA). The hardness and Young's modulus of the samples were measured *via* the CSM method using a Berkovich indenter tip. The substrate effects were eliminated by ensuring that the depth of all the indentations did not exceed one-tenth of the total thickness of the films.

3. Results and discussion

3.1 Design and synthesis of the FAP/$CaCO_3$ heterogeneous structured composites

Fig. 1a shows the fabrication procedure of the FAP/$CaCO_3$ heterogeneous structures inspired by teeth. Briefly, 1 wt% chitosan (CS) solution was spin-coated onto a clean slide glass followed by immersion in sodium hydroxide solution (pH = 9) (see the Experimental section). The glass slide was then transferred into a Ca^{2+} solution with Mg^{2+} and PAA. Layered $CaCO_3$ was fabricated *via* slow dripping of a solution containing carbonate ions using a peristaltic pump. Subsequently, the $CaCO_3$ layer together with the underlying CS thin film was transferred into a Ca^{2+} solution again after being rinsed with purified water. After mineralization for 96 h using a peristaltic pump, enamel-like fluorapatite columnar nanorod arrays were successfully grown on the $CaCO_3$ layer.

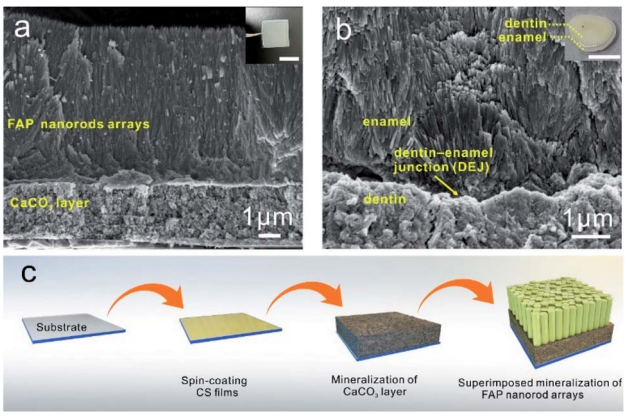

Fig. 1 Structure of the FAP/$CaCO_3$ heterogeneous composites and their biogenic counterparts and schematic illustration of the preparation process. (a) Cross-sectional SEM image of the FAP/$CaCO_3$ heterogeneous structured composites showing the underlying $CaCO_3$ layer and upper columnar fluorapatite nanorod arrays. Inset shows an optical photo of the sample; scale bar, 1 cm. (b) Cross-sectional SEM image of a human tooth. Inset shows an optical photo of a tooth slice; scale bar, 1 cm. (c) Schematic illustration of the preparation of the FAP/$CaCO_3$ heterogeneous structured composites.

The cross-sectional scanning electron microscopy (SEM) characterization of the composite reveals a continuous, bi-layered heterogeneous structured thin film with a uniform thickness of approximately 9 μm (Fig. 1a). The synthetic films show remarkable structural similarity to their biogenic counterpart (Fig. 1b). The detailed sketch of a human tooth is shown in Fig. S1.† Fig. 1a reveals a clear interface between the underlying $CaCO_3$ layer and the upper columnar fluorapatite nanorod arrays. The scanning electron microscopy (SEM) images show that the structure of the $CaCO_3$ layers is composed of about 50 nm nanoparticles that are tightly bonded by organic matter. The average thickness of the $CaCO_3$ layers was 3 μm. The morphology of the $CaCO_3$ layers before the mineralization of calcium phosphate is shown in Fig. S2.† The surface of the $CaCO_3$ layer is very smooth, and it is composed of 50 nm nanoparticles, which indicates that it maintains its original structure in the process of further mineralization. The calcium carbonate layer's surface is very flat, which provides a good condition for the superimposed mineralized FAP nanorod array layer. The upper columnar fluorapatite arrays comprise highly oriented thin nanorods that were tightly bound without any gaps. Near the interface, the FAP layer shows a granular structure, and the rod structure becomes more obvious as the height increases. This granular transition structure means that the $CaCO_3$ layers and FAP columnar layer are closely bound. The average thickness of the fluorapatite layer is approximately 6 μm.

In order to explore the influencing factors of interfacial interaction of the heterostructure and find the best synthetic strategy, $CaCO_3$/FAP heterogeneous structured composites were also synthesized (Fig. S3†). We first mineralized a layer of FAP columnar nanorod arrays after 96 h using a peristaltic pump, and then, mineralized layered $CaCO_3$ was superimposed on the FAP arrays. The planar SEM images show that the upper $CaCO_3$ layer is composed of 30 nm nanoparticles and the surface is flat (Fig. S3a and b†). The cross-sectional SEM images reveal that a 2 μm thick calcium carbonate layer was grown on the FAP arrays. However, the combination of the two layers at the interface is not closed. The gap of the nanorods at the interface is not filled by the nanoparticles of calcium carbonate, leaving a relatively large gap. This is because the surface roughness of the nanorod array is considerable, and the calcium carbonate layer is difficult to coat closely at the interface.

Fig. 2a presents the X-ray diffraction (XRD) patterns of the original $CaCO_3$ layers (red line) and FAP/$CaCO_3$ heterogeneous structured composites (blue line). The characteristic peak detected at 29.5° in the XRD pattern of the $CaCO_3$ layers was the (104) diffraction peak of calcite, and all the remaining diffraction peaks correspond to calcite. In the XRD pattern of the FAP/$CaCO_3$ composites (blue line), the characteristic peak detected at 26.0° corresponded to fluorapatite, and the characteristic peak of calcite disappeared. This means that the FAP nanorod array entirely covers the original calcium carbonate layer in the

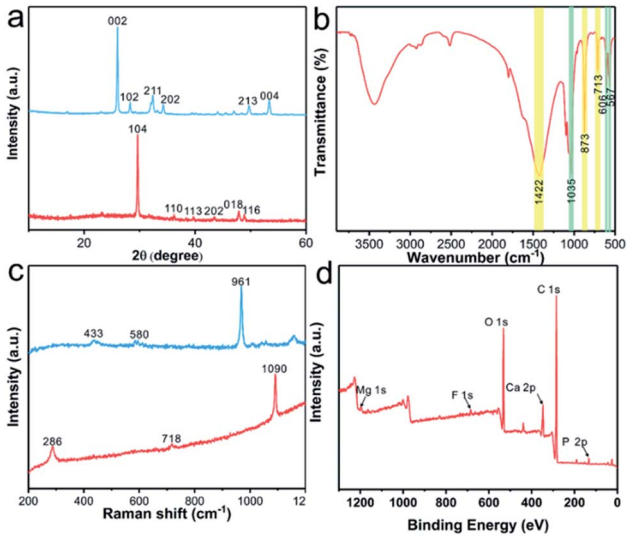

Fig. 2 (a) XRD patterns of the $CaCO_3$ layer (red line) and FAP/$CaCO_3$ heterogeneous structured composites (blue line). (b) FT-IR spectra of the FAP/$CaCO_3$ heterogeneous structured composites. (c) Raman spectra of the $CaCO_3$ layer and FAP/$CaCO_3$ heterogeneous structures composites. (d) XPS survey spectrum of the FAP/$CaCO_3$ heterogeneous structured composites.

second mineralization step. When there are holes in the FAP array, calcite and fluorapatite diffraction peaks appear simultaneously (Fig. S4†). Moreover, the intensities of the (002) diffraction peaks were significantly higher than those of the other diffraction peaks, thereby demonstrating preferential growth of the FAP nanorod arrays along the *c*-axis. This was consistent with the results of the SEM analysis. In the FT-IR spectra of the FAP/$CaCO_3$ heterogeneous structured composites (Fig. 2b), the asymmetric stretching in the vibration band of the C–O group appeared at 1422 cm^{-1}, and the peaks around 873 cm^{-1} and 713 cm^{-1} correspond to deformation in the vibration bands of the C–O group in calcite.[19,20] The bands at 567 cm^{-1} and 606 cm^{-1} correspond to the $\nu 4$ bending modes of PO_4^{3-}.[21] In addition, the band at approximately 1035 cm^{-1} corresponded to the $\nu 3$ bending mode of PO_4^{3-}.[22] Fig. 2c shows the Raman spectra of the $CaCO_3$ layers (red line) and FAP/$CaCO_3$ heterogeneous structured composites (blue line). The characteristic peaks at 286, 718, and 1090 cm^{-1} are the characteristic peaks of calcite.[23] The high-intensity characteristic peak at 961 cm^{-1} was indicative of the highly ordered FAP crystalline arrays. The XPS spectra (Fig. 2d) were analyzed to acquire the chemical status of the FAP/$CaCO_3$ composites. The XPS spectrum of the composites exhibits peaks corresponding to O, P, Ca, C, F, and Mg, revealing the presence of $CaCO_3$ and $Ca_5(PO_4)_3F$ in the composites. The high-resolution XPS profiles are presented in Fig. S5.† The C 1s spectrum can be divided into three peaks located at the binding energies of 288.80 eV, 286.1 eV and 284.8 eV, which are respectively attributed to CO_3^{2-} and the oxygen-bound bonds C–(O, N) and C–C.[24,25] The Ca 2p spectrum consists of two peaks with binding energies of 350.8 and 347.3 eV, corresponding to Ca $2p_{1/2}$ and Ca $2p_{3/2}$, which are in agreement with the Ca^{2+} oxidation state.[26,27] The F 1s spectrum exhibits a symmetric peak at 684.5 eV (Fig. S5†).[28] The P 2p spectrum presents two deconvoluted peaks at 132.9 and 134 eV,[29,30] (Fig. S5†) and almost no magnesium was detected because of its negligible amount.

Fig. 3 shows the SEM-EDS mapping of the FAP/$CaCO_3$ heterogeneous structured composites. Fig. 3a shows the heterogeneous structures of the underlying layered $CaCO_3$ and upper columnar fluorapatite nanorod arrays. Fig. 3b–g present the EDS mapping of O, F, P, C, Mg, and Ca. In the elemental distribution of P, O, and C, we can see an obvious dividing line between FAP and $CaCO_3$. There are more O and C and less P atoms in the $CaCO_3$ layer than in the FAP arrays. The content of each element is shown in Fig. 3h.

In order to reveal the internal structure of the FAP/$CaCO_3$ heterogeneous structured composite, the samples were treated with a focused ion beam (FIB). Fig. 4a shows the boundary between the $CaCO_3$ layer and FAP layer. It can be found that near the boundary, the FAP layer shows a granular structure, where the particle size is about 20 nm, and the rod structure becomes more obvious as the height increases (Fig. 4b). The red, yellow and blue boxes show the details of the $CaCO_3$ layer, the FAP granular transition area and the FAP nanorod array area, respectively (Fig. 4c–h). The underlying layer is $CaCO_3$ assembled by nanoparticles (Fig. 4c and d). The high-resolution transmission electron microscopy (HRTEM) image shown in Fig. 4d and the inset selected area electron diffraction (SAED) pattern shows that the small particles in the calcium carbonate layer crystallized very well. The upper layer is the FAP layer with a granular region and arrays in a closely arranged columnar structure. HRTEM images are also shown in Fig. 4f and h. The nanorods in the FAP layer exhibit single-crystal properties (Fig. 4h).

3.2 Mechanical properties of the FAP/$CaCO_3$ heterogeneous structured composites

Nanoindentation measurements were employed to measure the hardness (*H*) and Young's modulus (E_Y) values of the synthetic

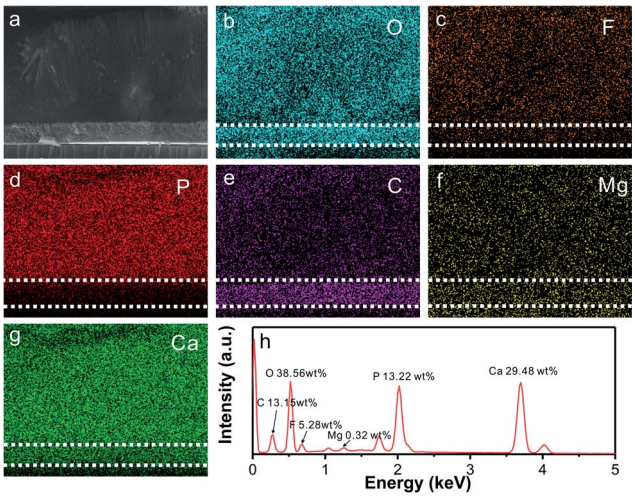

Fig. 3 SEM image (a), EDS mapping (b–g) and EDS profile (h) of the FAP/$CaCO_3$ heterogeneous structured composites.

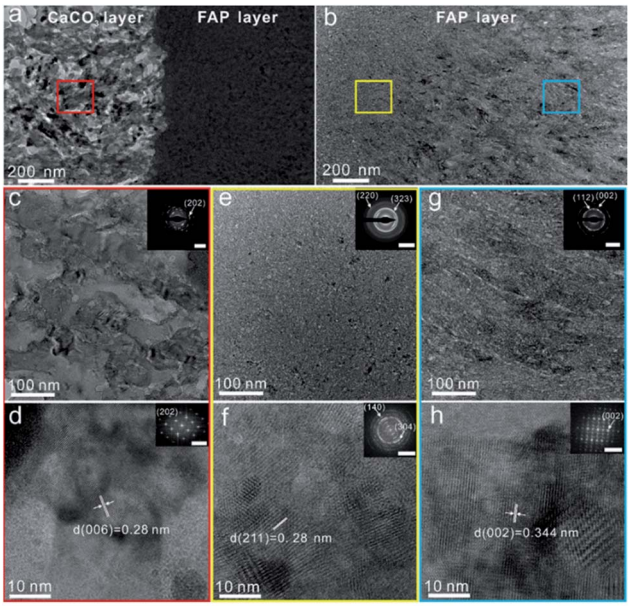

Fig. 4 Internal structure of the FAP/$CaCO_3$ heterogeneous structured composites. (a and b) The boundary of the FAP/$CaCO_3$ heterogeneous structured composites (red, yellow and blue boxes represent the $CaCO_3$ layer, FAP granular transition area and FAP nanorod array area, respectively). (c and d) Microstructure of the underlying $CaCO_3$ layer. (e and f) Microstructure of the FAP granular transition area. (g and h) Microstructure of the upper columnar fluorapatite nanorod arrays. Insets in (c, e and g) show the selected area electron diffraction patterns and insets in (d, f, and h) show the corresponding FFT patterns; scale bar, 5 nm^{-1}.

FAP/$CaCO_3$ heterogeneous structured composites. In order to avoid substrate and surface effects, the H and E_Y of our composites were measured by the continuous stiffness measurement (CSM) method with Berkovich probes at a depth of 900 nm, which did not exceed 10% of the total thickness. The synthetic FAP/$CaCO_3$ heterogeneous structured composite films exhibit H and E_Y values of 1.99 ± 0.02 GPa and 47.5 ± 0.6 GPa, respectively (Fig. 5a and b), which were comparable to those of natural teeth. These properties should be attributed to the structural continuity between the FAP layer and the $CaCO_3$ layer. When the whole composite is subjected to an external force, energy will pass through the nanorod array to the granular calcium carbonate layer with higher organic content (4.5 wt%) than that in the FAP arrays (Fig. S6†), and dissipate more energy to prevent the whole material from being destroyed. The synthetic FAP/$CaCO_3$ heterogeneous structured composites contain as much as 96.6 wt% inorganic components, which is quite comparable to that of natural teeth. Load–displacement curves are shown in Fig. S7.† Since the FAP arrays are arranged more closely, the mechanical properties of these synthetic FAP/$CaCO_3$ heterogeneous structured composites are lower than that of FAP arrays.[31] Table S1† presents other synthetic calcium phosphate and calcium carbonate materials.

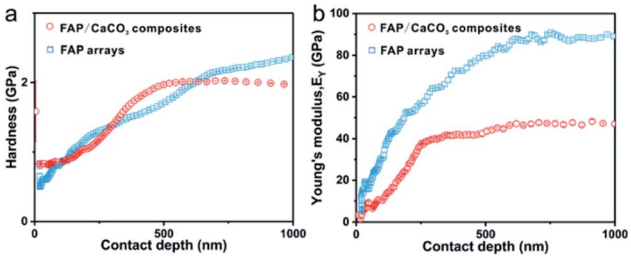

Fig. 5 Mechanical properties of the FAP/$CaCO_3$ heterogeneous structured composites and the FAP arrays tested by nanoindentation. (a) Hardness–displacement curves. (b) Young's modulus–displacement curves.

4. Conclusions

In summary, FAP/$CaCO_3$ heterogeneous structured composites with a tooth-like structure were successfully fabricated using a three-step mineralization method under ambient temperature. Inspired by the hierarchical architecture of teeth, we firstly grew a calcite calcium carbonate layer on the surface of chitosan (CS) films under the coordinated control of magnesium ions (Mg^{2+}) and polyacrylic acid (PAA). Subsequently, we grew FAP columnar nanorod arrays on the calcium carbonate layer *via* superimposed mineralization. The granular transition structure near the interface means that the $CaCO_3$ layers and FAP columnar layer are closely bound. The granular calcium carbonate layer with higher organic content (4.5 wt%) than that of the FAP arrays (3.4 wt%) can dissipate more energy to prevent the whole material from being destroyed. The hardness and Young's modulus of the synthetic FAP/$CaCO_3$ heterogeneous structured composites are 1.99 ± 0.02 GPa and 47.5 ± 0.6 GPa, respectively, which are comparable to those of natural teeth. We expect that this general strategy has broad applicability for preparing various multi-scale heterogeneous structured composite materials with unique functionalities under ambient conditions.

Author contributions

Li YD conducted the experiments and wrote the paper. Wang K and Fu ZY supervised the project. Zhou ZY, Ping H and Xie JJ guided the theoretical analysis part. Lei LW and Wang WM revised the paper. All authors contributed to the general discussion.

Conflicts of interest

There are no conflicts to declare.

Acknowledgements

This work was financially supported by the National Key Research and Development Program of China (2021YFA0715700) and the National Natural Science Foundation of China (51832003). The authors would like to thank Miss Ting-ting Luo (Center for Materials Research and Analysis, Wuhan University of Technology) for her help in the HRTEM analysis.

Notes and references

1 M. J. Buehler, *Nano Today*, 2010, **5**, 379–383.
2 G. X. Gu, M. Takaffoli and M. J. Buehler, *Adv. Mater.*, 2017, **29**, 1700060.
3 W. Yang, H. Quan, M. A. Meyers and R. O. Ritchie, *Matter*, 2019, **1**, 1557–1566.
4 E. A. Zimmermann, B. Gludovatz, E. Schaible, N. K. Dave, W. Yang, M. A. Meyers and R. O. Ritchie, *Nat. Commun.*, 2013, **4**, 1–7.
5 X. Li, W.-C. Chang, Y. J. Chao, R. Wang and M. Chang, *Nano Lett.*, 2004, **4**, 613–617.
6 C. Xiao, M. Li, B. Wang, M.-F. Liu, C. Shao, H. Pan, Y. Lu, B.-B. Xu, S. Li and D. Zhan, *Nat. Commun.*, 2017, **8**, 1–9.
7 J. J. Xie, H. Ping, T. N. Tan, L. W. Lei, H. Xie, X. Y. Yang and Z. Y. Fu, *Prog. Mater. Sci.*, 2019, **105**, 100571.
8 S. Mann, *Biomineralization: Principles and Concepts in Bioinorganic Materials Chemistry*, Oxford University Press on Demand, 2001.
9 W. D. Kingery, H. K. Bowen and D. R. Uhlmann, *Introduction to Ceramics*, John Wiley & Sons, 1976.
10 L. Wu, Y. Li, Z. Fu and B.-L. Su, *Natl. Sci. Rev.*, 2020, **7**, 1667–1701.
11 A. R. Studart, F. Filser, P. Kocher and L. J. Gauckler, *Dent. Mater.*, 2007, **23**, 106–114.
12 J. R. Kelly, *Annu. Rev. Mater. Sci.*, 1997, **27**, 443–468.
13 L. H. He and M. V. Swain, *J. Mech. Behav. Biomed. Mater.*, 2008, **1**, 18–29.
14 C. Chen, Z. Wang, M. Saito, T. Tohei, Y. Takano and Y. Ikuhara, *Angew. Chem.*, 2014, **126**, 1569–1573.
15 S. Bentov, P. Zaslansky, A. Al-Sawalmih, A. Masic, P. Fratzl, A. Sagi, A. Berman and B. Aichmayer, *Nat. Commun.*, 2012, **3**, 1–7.
16 R. Wang, L. Addadi and S. Weiner, *Philos. Trans. R. Soc. London, Ser. B*, 1997, **352**, 469–480.
17 B. Yeom, T. Sain, N. Lacevic, D. Bukharina, S.-H. Cha, A. M. Waas, E. M. Arruda and N. A. Kotov, *Nature*, 2017, **543**, 95–98.
18 J. Wei, H. Ping, J. Xie, Z. Zou, K. Wang, H. Xie, W. Wang, L. Lei and Z. Fu, *Adv. Funct. Mater.*, 2020, **30**, 1904880.
19 D. Azizi and F. Larachi, *Colloids Surf., A*, 2018, **537**, 126–138.
20 T. Wang, B. Feng, Y. Guo, W. Zhang, Y. Rao, C. Zhong, L. Zhang, C. Cheng, H. Wang and X. Luo, *Miner. Eng.*, 2020, **159**, 106635.
21 K. Tank, P. Sharma, D. Kanchan and M. Joshi, *Cryst. Res. Technol.*, 2011, **46**, 1309–1316.
22 L. Berzina-Cimdina and N. Borodajenko, *Infrared Spectrosc.: Mater. Sci., Eng. Technol.*, 2012, **12**, 251–263.
23 I. K. Shaik, L. Zhang, S. Pradhan, A. K. Kalkan, C. P. Aichele and P. K. Bikkina, *J. Pet. Sci. Eng.*, 2021, **198**, 108231.
24 J. Yang, J. Cui, A. Xie, J. Dai, C. Li and Y. Yan, *Colloids Surf., A*, 2021, **608**, 125583.
25 F. Scalera, A. G. Monteduro, G. Maruccio, L. Blasi, F. Gervaso, E. Mazzotta, C. Malitesta and C. Piccirillo, *Sustainable Mater. Technol.*, 2021, **28**, e00260.
26 S. Sun, H. Ding, X. Hou, D. Chen, S. Yu, H. Zhou and Y. Chen, *Appl. Surf. Sci.*, 2018, **456**, 923–931.
27 H. Xiong, J. Chen, T. Zhang, W. Wang, C. Huang, Y. Zhu and B. Hu, *J. Mol. Liq.*, 2021, **322**, 114986.
28 J. Xu and K. A. Khor, *J. Inorg. Biochem.*, 2007, **101**, 187–195.
29 C. L. Popa, A. Deniaud, I. Michaud-Soret, R. Guégan, M. Motelica-Heino and D. Predoi, *J. Nanomater.*, 2016, 1062878.
30 J. Wu, K. Ueda and T. Narushima, *Mater. Sci. Eng., C*, 2020, **109**, 110599.
31 Y. D. Li, H. Ping, J. J. Wei, Z. Y. Zou, P. C. Zhang, J. J. Xie, Y. H. Jia, H. Xie, W. M. Wang, K. Wang and Z. Y. Fu, *ACS Appl. Mater. Interfaces*, 2021, **13**, 25260–25269.